Diamond & Related Materials 23 (2012) 66–71

Contents lists available at SciVerse ScienceDirect

Diamond & Related Materials

journal homepage: www.elsevier.com/locate/diamond

In-situ deposition of sparse vertically aligned carbon nanofibres on catalytically activated stainless steel mesh for field emission applications

M.T. Cole [a,*], K. Hou [a,1], J.H. Warner [b], J.S. Barnard [c], K. Ying [a], Y. Zhang [a], C. Li [a,d], K.B.K. Teo [e], W.I. Milne [a,f]

[a] *Electrical Engineering Division, Department of Engineering, University of Cambridge, 9 JJ Thomson Avenue, Cambridge, CB3 0FA, United Kingdom*
[b] *Department of Materials, University of Oxford, Parks Road, Oxford, OX1 3PH, United Kingdom*
[c] *Department of Materials Science & Metallurgy, University of Cambridge, Pembroke Street, Cambridge, CB2 3QZ, United Kingdom*
[d] *School of Electronic Science & Engineering, Southeast University, Nanjing, 210096, China*
[e] *AIXTRON Ltd., Swavesey, CB24 4FQ, United Kingdom*
[f] *Department of Information Display, Kyung Hee University, Seoul, 130701, South Korea*

ARTICLE INFO

Article history:
Received 19 July 2011
Received in revised form 21 December 2011
Accepted 22 December 2011
Available online 14 January 2012

Keywords:
Carbon nanofibres
Field emission
Coatings
Electrochemical processing

ABSTRACT

We report on an inexpensive, facile and industry viable carbon nanofibre catalyst activation process achieved by exposing stainless steel mesh to an electrolyzed metal etchant. The surface evolution of the catalyst islands combines low-rate electroplating and substrate dissolution. The plasma enhanced chemical vapour deposited carbon nanofibres had aspect-ratios > 150 and demonstrated excellent height and crystallographic uniformity with localised coverage. The nanofibres were well-aligned with spacing consistent with the field emission nearest neighbour electrostatic shielding criteria, without the need of any post-growth processing. Nanofibre inclusion significantly reduced the emission threshold field from 4.5 V/μm (native mesh) to 2.5 V/μm and increased the field enhancement factor to approximately 7000.

1. Introduction

Porous metal mesh substrates are mechanically flexible, partially transparent, and have high thermal and electrical conductivities. Carbon nanofibres (CNFs), high aspect-ratio allotropes of sp^2-bonded carbon, are optically, mechanically and electrically unique. One of the most important applications of such materials is in cold cathode field emission. CNFs dramatically enhance a substrate's field emission performance, though weak adhesion and poor electronic transparency at the substrate interface result in fibre de-anchoring and substantial resistive losses. Direct *in-situ* CNF synthesis introduces arrays of well-anchored tips [1,2] and ultimately facilitates the development of many novel low-end field emission applications, such as flexible conducting field emitters for environmental lighting, for example.

The main strategies for composite fabrication are *ex-situ* coating and *in-situ* deposition. In *ex-situ* coating a variety of binding materials adhere pre-grown nanostructures to arbitrary substrates [3,4]. CNFs are homogenously dispersed into binders, such as Teflon and Nafion, via damaging acid treatments and ultrasonication, and then cast, sprayed, or dip deposited. However, CNF immobilisation occludes much of the field emitting surface thereby reducing the emission performance. Uniform alignment is not possible. *In-situ* deposition negates these detrimental features. Transition metal catalysts are powder [5], slurry [6] or vacuum deposited [7]. Pre-formed nanoparticle suspensions require considerable post-processing and, in practice, during their filtration and preparation experience significant losses in the available catalytically active species due to attrition [8]. Vacuum processes obviate this, but are comparatively costly and particularly time consuming. Most studies on the *in-situ* growth of CNFs on metallic substrates detail the growth of highly disordered and unaligned networks and have focused, almost exclusively, on catalyst deposition or surface preparation via physical abrasion and thermal oxidation [9,10,8].

Kanthal, an iron-chromium-aluminium alloy, [11,12], Inconel [13] and Nichrome/Chromel [14] have shown some promise, though are all more than one order of magnitude more expensive per unit volume than stainless steel. Moreover, the catalyst in these studies was typically solution or vapour-phase deposited iron nitrate salts rather than direct activation of the intrinsic catalyst available in the bulk substrate [15]. Masarapu et al. [16] reported unaligned CNF synthesis on stainless steel foil using strong acid dip processes. However, as with previous studies, the resulting CNFs were randomly aligned and spaghetti-like in morphology which degrades the field emission performance. The few studies that achieved vertically aligned nanostructures typically produced conformal and dense forests which offered low field emission performance. For optimal field emission, sparse arrays are desirable. Nilsson et al. [17] and Groening et al. [18] showed

* Corresponding author. Tel.: +44 1223 748329.
E-mail address: mtc35@cam.ac.uk (M.T. Cole).
[1] Present address: Research Center, State Grid Electric Power Research Institute, Nanjing 210003, China.

0925-9635/$ – see front matter.
doi:10.1016/j.diamond.2011.12.039

Table 1
Typical bulk composition of the as-received ss-mesh.

wt.% Fe	wt.% Cr	wt.% Ni	wt.% O	wt.% Mn	wt.% Si
64.40	18.86	8.30	4.04	2.40	2.00

that the optimal array geometry of vertically aligned nanotubes and nanofibres, in order to minimise nearest neighbour electrostatic shielding, requires a pitch approximately twice the emitter's height. High density forests have nanometer-scale spacing and therefore require exceptionally short emitters. However, short CNFs have a significantly reduced field enhancement factor. Evidently, sparse vertically aligned CNFs are necessary to provide high performance field emission characteristics. In light of this it becomes apparent that there has been very limited success in producing the required geometrically defined vertically aligned CNF arrays through low-cost means on Fe- and Ni-containing alloys.

An industry compatible alternative for the direct-deposition of highly-aligned, sparse CNFs on metallic substrates is necessary. Catalysis activation, of low-cost and widely available Fe-, Ni or Co-containing metallic supports, through single-step electrochemical reactions, offers one possible solution. The technique presented here offers high levels of homogeneity, superior alignment and excellent inter-CNF spacing, which have yet to be demonstrated elsewhere. In this paper we consider the underlying catalyst activation process and investigate the field emission properties of the resulting CNF/ss-mesh composite. Our results establish a feasible, reliable, and scalable approach to the fabrication of low-end, flexible and porous field emitters.

2. Experimental details

Type 304 stainless steel (ss)-mesh (Alfa Aesar, 36% pitch, 50 μm diameter) was selected as the catalyst-containing substrate. The typical bulk composition is detailed in Table 1. Preliminary scanning electron microscopy (SEM) analysis on etchant exposed samples showed negligible surface alteration. An electrochemical approach was used to accelerate the surface preparation. 20×20-mm-samples were connected to a simplified potentiostat, as shown in Fig. 1(a). Unless otherwise stated, the ss-mesh formed the cathode (CNF growth substrate) and the driven anode. No polymer passivation was applied to the driven electrode. The analyte was a commercially available metal etchant (Michrochem), nominally composed of phosphoric acid (66.3–70.3 wt.%), acetic acid (8.7–10.7 wt.%) and nitric acid (1.5–2.0 wt.%). The analyte was diluted to 1:1 with de-ionised (DI) water, and agitated for 10 min. Samples were exposed to the solution for 10 s (zero bias) for dynamic stabilisation followed by the application of a direct-current (d.c.) bias to initiate the surface pre-treatment.

CNFs were synthesised by plasma enhanced chemical vapour deposition (PE-CVD) performed in a cold-walled commercially available reactor (AIXTRON Ltd.). Samples were annealed for 30 s on a resistively heated low-mass graphite stage ramped to 600 °C at 5 °C/s. To initiate growth the stage was heated to 850 °C, and 200 sccm NH_3

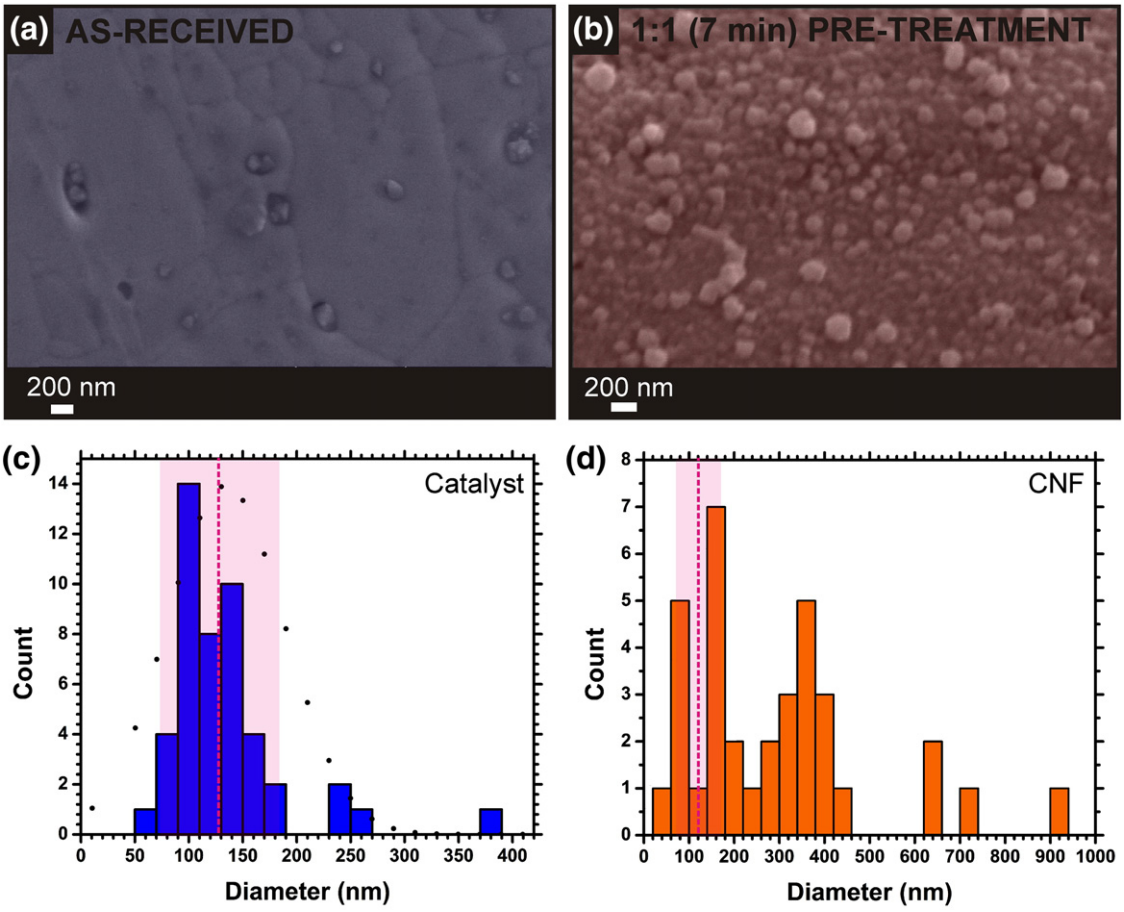

Fig. 1. Comparative SEM micrographs (false coloured) of (a) the as-received ss-mesh and (b) the ss-mesh after electrolysing pre-treatment. (c) Histogram of the catalyst diameter after a 7 min pre-treatment in a 1 (DI):1 (Etchant) solution at 250 V/m. Fitted Normal distribution showing a mean catalyst diameter of 125 ± 55 nm (± 1 S.D), as depicted. Few catalyst islands smaller than 40 nm were observed. (d) CNF diameter distribution (7 min pre-treatment) showing a nominal Bimodal distribution with a dominant peak at 120 ± 50 nm (± 1 S.D). Note the strong correlation between the mean catalyst diameter (125 nm) and mean CNF diameter (120 nm).

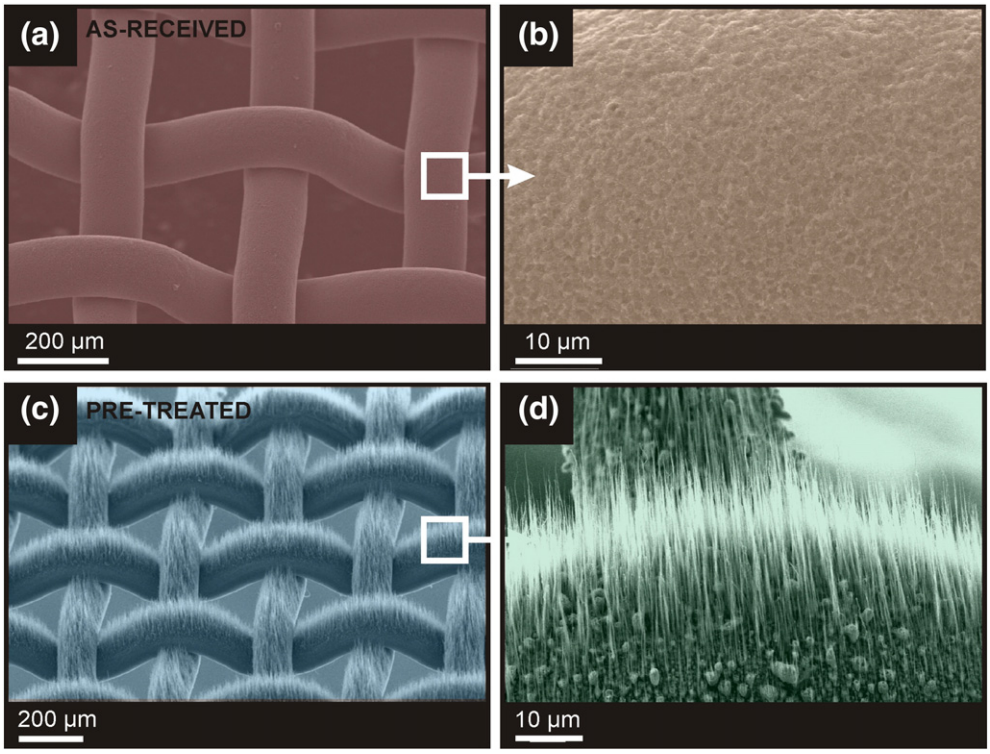

Fig. 2. SEM micrographs following PE-CVD CNF synthesis. (a, b) As-received ss-mesh. No CNF growth observed. (c, d) CNF/ss-mesh composite where the catalyst bed was prepared by the electrolyzed etchant pre-treatment.

and 55 sccm C_2H_2 were introduced, at 5 mbar, with a glow-discharge plasma (640 $V_{d.c.}$, 45 W). After 20 min growth was terminated by evacuating the chamber to 2×10^{-2} mbar and cooling to ambient under 200 sccm N_2.

High resolution scanning and transmission electron microscopy (HR-SEM/TEM), select area electron diffraction (SAED) and energy-dispersive X-ray (EDX) spectroscopy were performed using a Carl Zeiss 50, a JEOL JEM-4000EX, and a Schottky field emitting FEI-Philips XL30, respectively. Crystallographic information was extracted using a Philips CM300 field emission-TEM and an aberration corrected FEI Titan^3 80-300 in scanning TEM mode with bright-field and annular dark-field detectors. Composition maps were recorded using a Hitachi S-5500 scanning transmission electron microscope (STEM) fitted with an Oxford Instruments EDX detector. Additional data on the graphitic structure was revealed spectroscopically using a Renishaw inVia, He–Ne laser, Raman spectrophotometer, operated at 633 nm, with an incident power of 3 mW. CNF alignment was ascertained using the Steradian 37 (Str37) function in the SPIP™ Metrology image analysis software (v. 5.15). Str37 is defined as the ratio of the in-plane distance between the real autocorrelation centre and the boundary at which the height of the image has decayed to 37% of the depth-range at said autocorrelation centre. An autocorrelation is applied to the images depth-range to infer this position. The decay in the depth-range in all directions is evaluated and the Str37 value is calculated [19,20]. For perfectly aligned arrays Str37 = 0, whilst for disordered networks, with exhibit no directional preference, Str37 = 1. Field emission measurements were performed using a custom-built, LABVIEW controlled ion-pumped vacuum

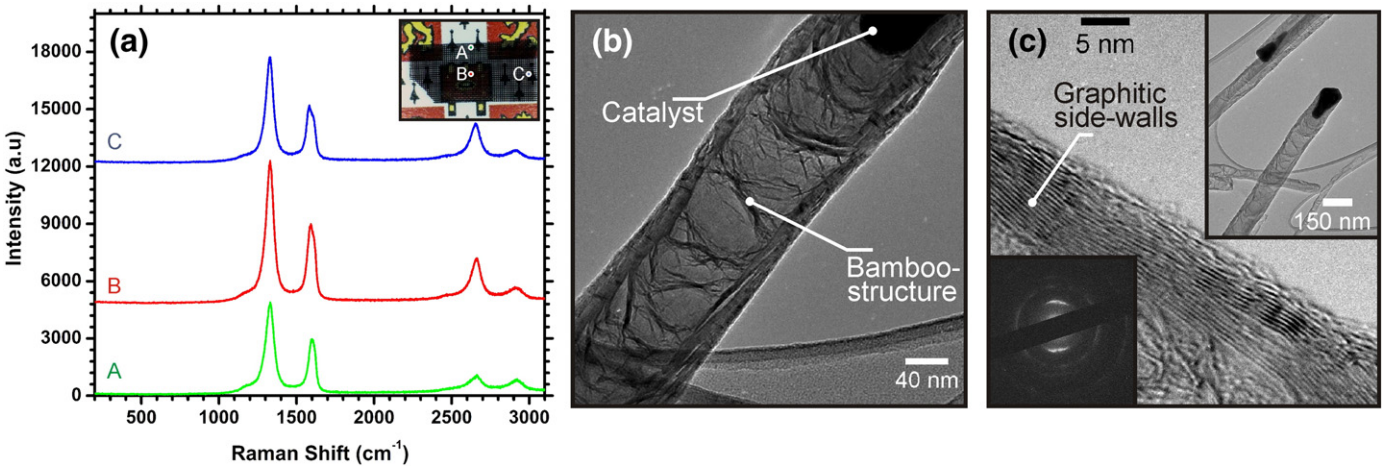

Fig. 3. (a) Raman spectra (633 nm excitation, 3 mW incident power) representing accumulations at positions A, B, C (*inset*). Intensity spectra (arbitrary units — a.u), are vertically displaced for clarity. (b) Typical HR-TEM micrograph of a synthesised CNF highlighting the bamboo-structure. (c) HR-TEM micrographs and SAED pattern (*lower left inset*) suggesting turbostratic alignment of the graphitic side-walls. The *upper right inset* shows a low-resolution TEM micrograph of a catalyst particle at a CNFs tip.

system connected to a 5 kV power supply and a HP 34401A source-metre. CNF/ss-mesh samples formed the cathode and an indium tin oxide coated glass slide formed the anode. Potentials were swept several times and emission characteristics were recorded on both the positive and negative incremental sweeps.

3. Results and discussions

3.1. In-situ CNF synthesis

Fig. 1(a, b) shows SEM micrographs of the as-received and pre-treated ss-mesh (1 (DI):1 (etchant), 7 min). Spherical structures, herein 'catalyst islands', 125 ± 55 nm (±1 S.D.) in diameter, conformally coat the electrochemically treated mesh (Fig. 1(c)). High magnification SEM showed few islands < 40 nm in diameter. Fig. 1(d) depicts the CNF diameter distribution (7 min pre-treatment) showing a dominant peak at 120 ± 50 nm (±1 S.D.), consistent with the initial catalyst diameter given the experimental uncertainties. Varying the pre-treatment duration coarsely controlled the catalyst island size, and the consequent CNF diameter. To demonstrate the commutability of the pre-treatment process, electrolysed mesh samples were exposed to various proven nanotube and nanofibre growth conditions. For example, 4% C_2H_2 diluted in a H_2 atmosphere (25 mbar) at 700 °C, resulted in a conformal coating of extremely dense aligned multi-walled nanotubes, 10.6 ± 4.7 nm (±1 S.D.) in diameter.

SEM micrographs, post PE-CVD, of the as-received and pre-treated ss-mesh are given in Fig. 2(a, b) and Fig. 2(c, d), respectively. No CNFs were observed on the as-received ss-mesh. Vertically aligned CNFs grew on the pre-treated samples only. Their nominal length and diameter were 10–50 μm (linear growth rate = 8–40 nm.s^{-1}) and 70–310 nm, giving typical aspect-ratios in excess of 150. The packing density and inter-CNF spacing were 4×10^8 cm^{-2} and 0.5–5.0 μm, respectively. Cross-sectional electron microscopy revealed a surface area coverage of approximately 42%. CNF/ss-mesh composites where flexed approximately 10^2 cycles through a bend radius of ~4 mm (10 mm × 10 mm samples). HR-SEM analysis confirmed a negligible loss in CNFs. However, the ss-mesh became increasingly brittle following the high-temperature processing. One way to ensure maintained mechanical stability of the ss-mesh substrate is to reduce both the synthesis temperature and thermal ramp.

Fig. 3(a) shows Raman spectra obtained under ambient conditions. Lorentzian fitting revealed D and G peaks at ~1329 cm^{-1} and ~1595 cm^{-1} — characteristic peaks associated with the first-order boundary phonon mode of defects within the bulk graphitic structure, and the radial carbon-carbon stretching mode of sp^2 bonds, respectively. An I_G/I_D ratio of 1.67–1.85, suggests the presence of nanoscale carbon clusters. Spectra were equivalent between central and peripheral regions, demonstrating the high levels of macroscopic uniformity in the pre-treatment process. A typical HR-TEM micrograph of a synthesised CNF is given in Fig. 3(b). The graphitic multi-walled CNFs are formed from 14 to 44 graphene planes with an inter-plane separation of ~0.39 nm (Fig. 3(c)). The characteristic circular features in the SAED pattern (lower inset, Fig. 3(c)) corroborate the crystallinity inferred from the Raman spectra, and the polycrystallinity associated with the multiple turbostratic graphitic side-walls [21]. The CNFs were formed from multiple defective bamboo-type sections spaced ~80 nm apart, and the electrochemically derived catalyst particles tended to reside at the tip (upper right inset, Fig. 4(a)). Lattice straining is evidenced in the dark field micrograph in Fig. 4(b). Combined STEM and EDX analysis implied a predominately Ni tip (Fig. 4(a, d)) with trace Fe. N was found throughout (Fig. 4(c)). Here, *a*-C was etched via the pyrolysis of NH_3, and liberated N has been shown to produce N-doped bamboo-like CNFs [22–24].

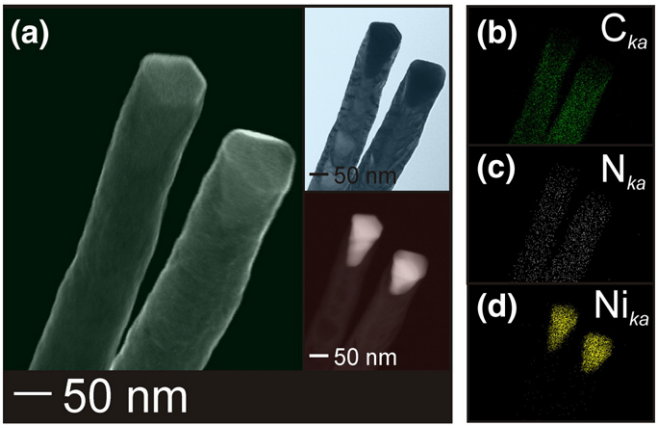

Fig. 4. (a) (False coloured) STEM micrographs of two PE-CVD synthesised CNFs and the corresponding bright field (*top inset*) and dark field (*bottom inset*) images highlighting the metallic tip and graphitic striations in the body of the nanofibre. (b–d) EDX maps showing strong C and N signatures throughout and a predominately Ni tip.

3.2. Mechanisms underlying catalyst bed evolution

The corrosion resistance of ss to nitric and phosphoric acids is well reported [25–27]. Standard potentiostats have been commonly employed, where the driven and measuring electrodes were polymer passivated. Hence the available data, and speculations therein, only partly explain the surface evolution observed here. To achieve the extent of surface roughness observed through dissolution alone necessitates very high dissolution rates. Such rates potentially exceed the liberation potential of the analyte, suggesting a concurrent surface evolution process. Two processes give rise to the observed surface topography: dissolution (or etching) and driven-precipitation (or low-rate electroplating). A complex relationship exists between the dissolution and electroplating. In a dissolution-type process, the pre-treatment increases the surface roughness and removes catalytically-poisonous materials [28]. Conversely, in low-rate electroplating the divalent transitional metal ions, the necessary CNF catalysts and primary constituents in the ss-mesh, liberated from the counter electrode (Fe or Ni foil, Advent-99.5%) and/or the ss-mesh itself, are deposited on the ss-mesh.

Electrolyzed pre-treatments were repeated using a graphite anode. Graphite was selected due to its excellent corrosion resistance to phosphoric and nitric acid [29] in addition to its negligible Fe, Ni or Co content (EDX data not shown) thereby removing possible electroplating during the pre-treatment. Characteristic globular catalyst islands were formed, as before, though much larger in size (560 ± 260 nm). No CNFs was observed upon PE-CVD. Thus, during the pre-treatment the analyte not only etches the ss-mesh but also, and perhaps more importantly, weakly electroplates.

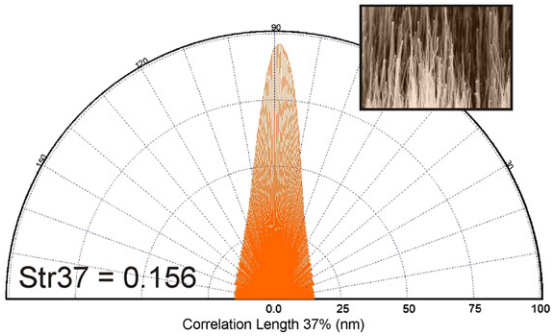

Fig. 5. Representative CNF alignment evaluated using the Str37 function in the SPIP™ image analysis software.

Nitric and phosphoric acids are strong oxidising agents. At exposed surfaces, the ss and foil counter electrode are oxidised and the Fe, Ni and Cr enter the analyte in their corresponding ionic form: Fe^{2+}, Ni^{2+} and Cr^{3+} [9]. The deposition of iron oxide on the ss-mesh occurs through a simultaneous dissolution and electroplating mechanism, where the presence of iron oxide is strongly evidenced by the orange discolouration of the ss-mesh upon air exposure. The detailed analyte composition was studied by EDX spectroscopy across a variety of pre-treatment times (10–600 s) and applied potentials (0–750 V/m). Consistently strong P (~19.4 wt.%), Si (~22.3 wt.%), C (~12.0 wt.%) and O (~46.3 wt.%) peaks were noted. More importantly, however, no Fe or Ni signatures were observed. The liberated catalyst materials, from both the ss-mesh and anode, have short residence times in the analyte and are efficiently redeposited. Cr and Ni oxides tend to nucleate directly on the ss-mesh [29]. At elevated temperatures during CNF synthesis, these metal oxides reduce and revert to their catalytically active form [9,30].

Phosphoric acid converts iron(III) oxide, formed on the ss-mesh via the action of the nitric acid, to catalytically inactive ferric phosphate; a reaction suggested by the green hue of the etchant during the pre-treatment. This passivation renders portions of the ss-mesh surface catalytically inactive and perhaps gives rise to the sparseness of the CNF arrays.

In principle, the conformal native oxide on the as-received ss-mesh can be similarly reduced to form active catalyst sites. However, this native oxide is often substantially thinner (<3 nm) than the electrochemically oxidised surface and the activation proceeds through an inefficient tertiary oxidation-reduction-growth process during PE-CVD. During reduction, the immobile native oxide does not readily form into catalyst islands. Thus, although catalyst materials are accessible, suitable catalyst topographies are not. The electrochemical pre-oxidation step enhances the surface roughness and removes the need for surface mobilisation during reduction and is, as a result, critical in CNF nucleation.

3.3. Field emission

For field emission applications, employing vertically aligned CNFs is critically important. Fig. 5 depicts the CNF alignment in this work evaluated using the Str37 function. Str37 = 0.91, 0.67, 0.29, and 0.16, for the works of Vander Wal et al. [9], Martinez-Hansen et al. [8] and this work (7/10 min pre-treatment), respectively, demonstrating the high-degree of CNF alignment achievable through our single-step electrochemical pre-treatment compared to other solid-state surface abrasion techniques. Nilsson et al. [17] and Groning et al. [18] determined that to minimise inter-CNF electrostatic shielding, thereby optimising the attainable field enhancement factor without

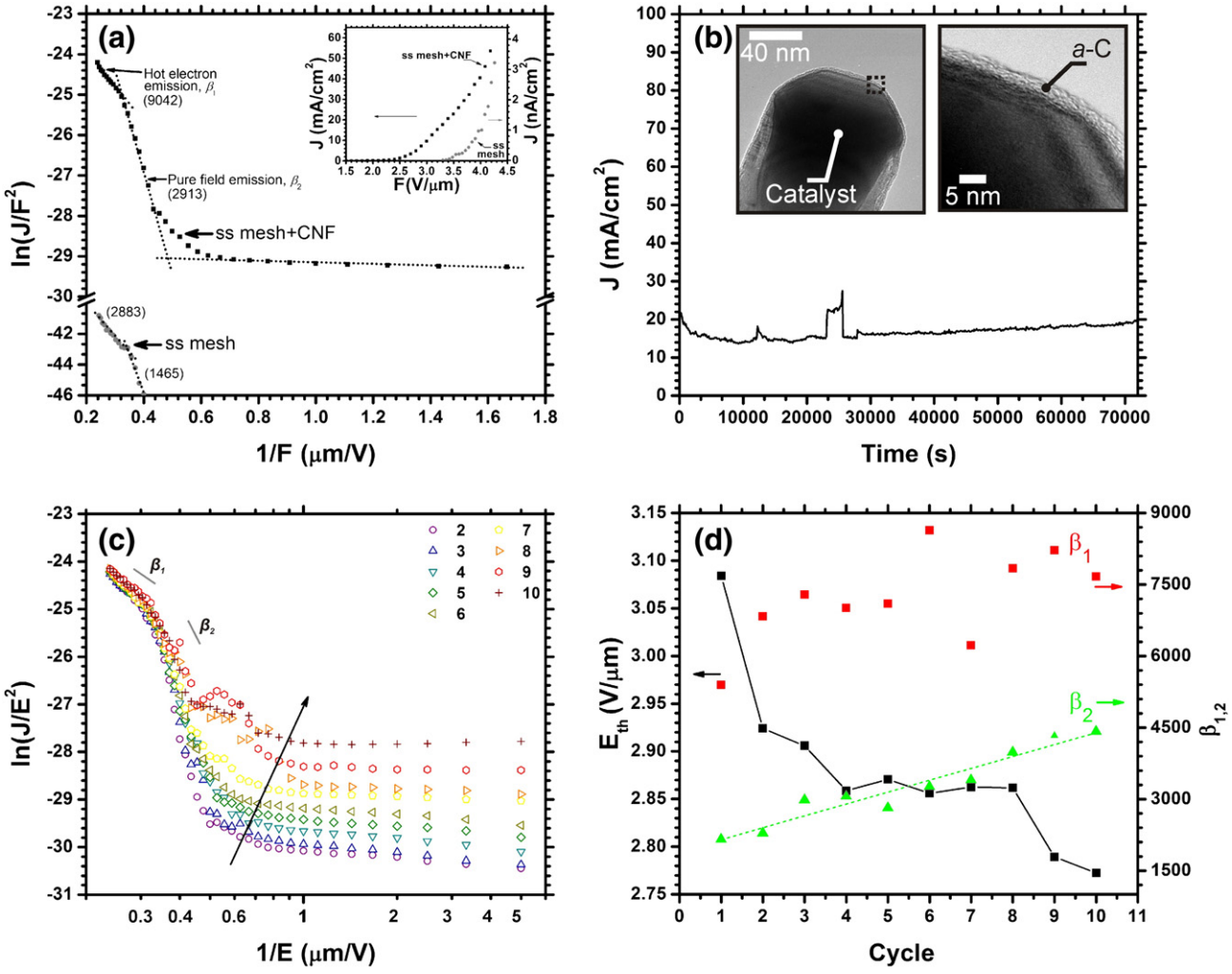

Fig. 6. Field emission characteristics of a 7 min electrolysed CNF/ss-mesh composite. (a) Comparative Fowler–Nordheim plot of the as-received ss-mesh and the CNF/ss-mesh composite. Data fitted using Eq. (1). *Inset*: electric-field (F) dependence of the emission current density (J). (b) Temporal stability conducted at 5×10^{-6} mbar. *Insets*: HR-TEM micrographs of an individual CNF tip. Metallic catalyst particles and *a*-C dominate the emission sites. (c) FN plot of the cyclic performance. (d) Variation in F_{th} (for an emission current of 6.25 mA/cm^2), β_1 and β_2 as a function of the cycle number.

compromising the emitted current density, the optimum pitch is approximately twice the CNF height. Indeed, here we see that the inter-CNF spacing is regulated by the electrochemical pre-treatment by the formation of ferric phosphate, and that for maximised field enhancement CNFs ~10 μm in length are required, which correlate well with our reported data.

The field emission characteristics of the as-received and CNF coated ss-mesh are plotted in Fig. 6. Fowler–Nordheim (FN) theory stipulates that the emitted current density J, under the influence of an applied electric field F, is;

$$J = \left(A\beta^2F^2/\phi\right)\exp\left(-B\phi^{3/2}/\beta F\right) \quad (1)$$

where $A = 1.54\times10^{-6}$ A eV V^{-2} and $B = 6.83\times10^{9}$ eV$^{3/2}$ V m^{-1} [31], β is a geometry dependent field enhancement factor and ϕ is the work function of the emitting surface, assumed to be 5.0 eV [32]. The emission characteristics are linear in the low-field regime and compare favourably with those of PE-CVD synthesised CNTs on less exotic substrates [32,33]. The inset in Fig. 6(a) shows the *J-F* plot. The corresponding FN plot has been fitted using Eq. (1). Two dominant emission regimes exist. The first is attributed to hot electron emission (β_1) [34] and the other to pure FN-type emission (β_2). CNF inclusion increases the native β_2 (where this 'native' enhancement is due to the cylindrical geometry of the ss-mesh fibres) by as much a factor of two, producing sufficiently large enhancement factors suitable for low-end field emission applications such as environmental lighting. Furthermore, CNF coatings significantly reduced the turn-on fields from 4.5 V/μm (as-received) to 2.5 V/μm.

Fig. 6(b) summarises an accelerated lifetime measurement performed at 10^{-6} mbar, with an initial emission current density of 20 mA/cm^2. Stable performance is observed. Modest spikes in the emission current are attributed to thermal destruction of CNFs caused by gas desorption lowering the local work function thereby significantly increasing the emitted current density and inducing substantial heating in the perturbed CNF. As shown in the insets of Fig. 6(b), *a*-C coats the emitters. *a*-C has a greater absorptive capacity than graphitic carbon [35] suggesting that the *a*-C residues initiate burn-out. We believe removal or thermal graphitisation of such *a*-C would improve the lifetime of the emitters and permit higher pressure functionality.

The cyclic stability is given in Fig. 6(c, d). The extraction field was cycled between 0 and 4 V/μm. The threshold field (F_{th}), for $J = 6.25$ mA/cm^2, decays and plateaus after a 10% reduction within 10 cycles. No functional relationship in β_1 was noted. The field enhancement factor in the pure FN regime (β_2) showed a strong positive correlation with cycle number. We believe this to be a result of increased uniformity across emission sites as dominant peaks are burnt off, thereby normalising, and increasing the global enhancement factor. Moreover, CNF removal increases the inter-CNF spacing which reduces the level of electrostatic shielding [36], and simultaneously reduces F_{th} whilst increasing β_2.

4. Conclusions

In the present study a simple, inexpensive route towards the *in-situ* deposition of vertically aligned CNFs on stainless steel mesh via catalyst activation is reported. Bamboo-like CNFs with aspect-ratios > 150 were synthesised. Electrochemical pre-treatment increases the surface roughness which encourages pre-oxidation and thermal reduction during CNF growth by PE-CVD. Combined etching and electroplating account for the evolution of the catalytically active surface. Field emission measurements showed substantial improvements in the field enhancement factors and turn-on fields following CNF deposition and temporally stable emission making the CNF/ss-mesh composites well suited for large-scale, low-end environmental lighting based on transition-metal-containing alloys.

Acknowledgements

M-T-C acknowledges the generous support of the Schiff Studentship, Cambridge University, and financial assistance from St. John's College, Cambridge and St. Edmund's College, Cambridge. M-T-C and K-H wish to thank Dr. M. Mann and Dr. D. G. Hasko for their fruitful discussions and experimental insight. C-L is grateful for the financial support of the Scientific Research Foundation, Southeast University, China (Grant No. YBJJ0926). The authors' thank the Cavendish Laboratory, Cambridge University, for the kind use of their SEM and Raman facilities.

References

[1] T. Hiraoka, T. Yamada, et al., J. Am. Chem. Soc. 128 (2006) 13338–13339.
[2] S.H. Jo, D.Z. Wang, et al., Appl. Phys. Lett. 85 (2004) 810–812.
[3] M.D. Rubianes, G.A. Rivas, Electrochem. Commun. 5 (2003) 689–694.
[4] J. Wang, M. Musameh, et al., J. Am. Chem. Soc. 125 (2003) 2408–2409.
[5] Y. Liu, W.Z. Qian, et al., Carbon 46 (2008) 1860–1868.
[6] S.H. Tang, G.Q. Sun, et al., J. Electrochem. Soc. 157 (2010) 1321–1325.
[7] C. Zhang, S. Pisana, et al., Diamond Relat. Mater. 17 (2008) 1447–1451.
[8] V. Martinez-Hansen, N. Latorre, et al., Catal. Today 147 (2009) 71–75.
[9] R.L. Vander Wal, L.J. Hall, Carbon 41 (2003) 659–672.
[10] L.Z. Gao, L. Kiwi-Minsker, et al., Surf. Coat.Technol. 202 (2008) 3029–3042.
[11] A. Rahaman, N. Patra, et al., Fullerenes Nanotubes Carbon Nanostruct. 16 (2008) 78–87.
[12] D. Sarangi, C. Hierold, et al., Fullerenes Nanotubes Carbon Nanostruct. 13 (2005) 243–254.
[13] S. Talapatra, S. Kar, et al., Nat. Nanotechnol. 1 (2006) 112–116.
[14] T. Chen, L.L. Wang, et al., Appl. Surf. Sci. 253 (2007) 7046–7049.
[15] P.M. Parthangal, R.E. Cavicchi, et al., Nanotechnology 18 (2007) 5 pp.
[16] C. Masarapu, B.Q. Wei, Langmuir 23 (2007) 9046–9049.
[17] L. Nilsson, O. Groening, et al., Appl. Phys. Lett. 76 (2000) 2071–2073.
[18] O. Groning, O.M. Kuttel, et al., J. Vac. Sci. Technol. B 18 (2000) 665–678.
[19] Z. Qinghui, P. Vichchulada, et al., Phys. Status Solidi A 207 (2010) 734–738.
[20] P. Vichchulada, Q.H. Zhang, et al., Appl. Mater. Interfaces 2 (2010) 467–473.
[21] Z. Jiong, J.M. Zuo, Carbon 47 (2009) 3515–3528.
[22] Y.T. Lee, N.S. Kim, et al., J. Phys. Chem. B 107 (2003) 12958–12963.
[23] K.B.K. Teo, S.B. Lee, et al., 3rd International Conference on Trends in Nanotechnology, Iop Publishing Ltd, Santiago Composte, Spain, 2002, pp. 204–211.
[24] C.P. Ewels, M. Glerup, J. Nanosci. Nanotechnol. 5 (2005) 1345–1363.
[25] J.Y. Jeng, B.E. Quayle, et al., Corros. Sci. 35 (1993) 1289–1296.
[26] E. Otero, A. Pardo, et al., Corros. Sci. 40 (1998) 1421–1434.
[27] V. Kain, S.S. Shinde, et al., J. Mater. Eng. Perform. 3 (1994) 699–705.
[28] V. Meille, Appl. Catal., A 315 (2006) 1–17.
[29] H. Iken, R. Basseguy, et al., Electrochim. Acta 52 (2007) 2580–2587.
[30] N.A. Jarrah, F.H. Li, et al., J. Mater. Chem. 15 (2005) 1946–1953.
[31] R. Seelaboyina, J. Huang, et al., Nanotechnology 18 (2007) 4840.
[32] C. Li, Y. Zhang, et al., Appl. Phys. Lett. 96 (2010) 143114–143117.
[33] S. Fujii, S. Honda, et al., Appl. Phys. Lett. 90 (2007) 1531081–1531083.
[34] M.J.G. Lee, Phys. Rev. Lett. 30 (1973) 1193–1196.
[35] H.H. Lowry, R.M. Bozorth, J. Phys. Chem. 32 (1928) 1524–1527.
[36] N. De Jonge, J.M. Bonard, Philos. Trans. R. Soc. Lond. A 362 (2004) 2239–2266.